

The evolutionary and asteroseismic imprints of mass accretion The $10 M_{\odot}$ β Cep case study

A. Miszuda¹ , Z. Guo² , and R. H. D. Townsend³ 

¹ Nicolaus Copernicus Astronomical Centre, Polish Academy of Sciences, Bartycka 18, PL-00-716 Warsaw, Poland
e-mail: amiszuda@camk.edu.pl, miszuda.amadeusz.astronomy@gmail.com

² Institute of Astronomy, KU Leuven, Celestijnenlaan 200D, B-3001 Leuven, Belgium

³ Department of Astronomy, University of Wisconsin-Madison, 475 N Charter St, Madison, WI 53706, USA

Received June 23, 2025

ABSTRACT

We investigate the structural and asteroseismic consequences of mass accretion in massive stars within close binary systems. Using MESA, we model the evolution of the $10 M_{\odot}$ accretor through and after a Roche lobe overflow phase. In addition to changing the surface composition of the star, mass accretion also significantly modifies the internal structure by expanding the convective core and altering chemical stratification near the core-envelope boundary. This partial core rejuvenation creates a distinct mean molecular weight gradient and leaves a persistent local density modulation.

In the late stages of mass transfer, changes in density and sound-speed profiles become apparent and influence stellar oscillations. We analyse the asteroseismic properties of the post-mass transfer models compared to single stars of the same mass and central hydrogen abundance. In the gravity mode regime, the altered Brunt-Väisälä frequency leads to period spacing patterns with larger amplitudes and phase shifts. For low- and intermediate-order pressure modes, we find systematic frequency deviations linked to changes in the sound-speed profile. Weight function analyses confirm that these differences arise primarily from structural modifications near the convective core boundary.

Furthermore, small frequency separations, sensitive to localized sound-speed gradients, reveal periodic variations attributable to the density discontinuity at the convective core edge. The accretor exhibits a larger sound-speed gradient integral and a longer acoustic radius ratio compared to the single star, consistent with its expanded core.

Our results demonstrate that mass accretion imprints measurable asteroseismic signatures on both gravity and pressure modes. These signatures provide powerful diagnostics for identifying post-interaction stars and for refining stellar age and structure estimates in binary systems.

Key words. binaries: close – stars: massive - stars: evolution – stars: interiors – stars: oscillations - asteroseismology – methods: numerical

1. Introduction

Binary stars constitute a significant fraction of the stellar population in the Galaxy. Observations indicate that over half of massive stars are born in binary or multiple systems (Duchêne & Kraus 2013; Sana et al. 2012), with possible interactions between components shaping their subsequent evolution. One of the key processes in such systems is mass transfer, which occurs when one star fills its Roche lobe and begins transferring material to its companion. This mass exchange profoundly alters both stars' evolution, often leading to rejuvenation, expansion and spin-up of one component or stripping of the other (Podsiadlowski et al. 1992; de Mink et al. 2013).

Mass transfer in close binaries leads to a range of structural and orbital consequences. As mass is accreted by the initially less massive star, the binary orbit responds according to the angular momentum conservation. The increasing mass of the accretor and corresponding mass ratio reversal typically result in orbital expansion during the later stages of the interaction (Soberman et al. 1997; Renzo et al. 2023). However initially, as noted by Renzo et al. (2019), the transfer of mass from the more massive donor causes the orbit to shrink. At the same time, the internal structure of the accreting star undergoes significant changes (Renzo & Götberg 2021). As material is deposited

onto the surface, it is gradually incorporated into the stellar interior through thermohaline, convective and rotational mixing processes, particularly near the core-envelope boundary (Neo et al. 1977). This mixing can supply the convective core with fresh hydrogen, effectively rejuvenating the star. The phenomenon of core rejuvenation leads to an increase in convective core mass and alters the subsequent nuclear burning history of the accretor. Moreover, the associated mixing processes can also alter the convective core size, internal chemical gradients, and rotational profile (Moe & Di Stefano 2017; Renzo & Götberg 2021). These changes in internal stratification have direct consequences for the star's pulsational properties (Guo 2021; Miszuda et al. 2022; Wagg et al. 2024; Henneco et al. 2024, 2025).

Asteroseismology offers a unique window into stellar interiors by analysing oscillation modes sensitive to different regions within the star (e.g., Aerts et al. 2010). In particular, gravity modes (g modes) probe stable, stratified regions, and specifically the chemical gradient and convective core boundaries, while pressure modes (p modes) provide constraints on the sound-speed profile in outer layers (Miglio et al. 2008). In mass-accreting stars, modifications to the internal structure due to accretion are expected to leave characteristic signatures in both g (Wagg et al. 2024; Henneco et al. 2024, 2025) and p mode fre-

quencies (Miszuda 2025). In particular, the rejuvenation from mass transfer shifts the p mode to higher frequencies (Guo et al. 2017) and the g mode period spacing to larger values (Guo & Li 2019). Arras et al. (2006) found that mass accretion can shift the edge of g mode instability strip of the white dwarf star in Cataclysmic Variables.

Recent observational and theoretical works have identified such asteroseismic signatures in post-mass transfer binaries. Studies of slowly pulsating B-type stars revealed period spacing deviations consistent with altered chemical profiles from mass accretion (Wagg et al. 2024). Similarly, models of pre-main sequence stars indicate that accretion histories shape their pulsational behaviour and internal structure (Zwintz & Steindl 2022).

In this work, we investigate the impact of mass accretion on the internal mixing, structure, and pulsational properties of massive, $10 M_{\odot}$ accretor stars using detailed binary evolution modelling. By comparing accretor models with single-star counterparts, we identify key structural changes and their observational consequences, advancing the understanding of the role of mass transfer in stellar evolution.

2. Methodology

2.1. Evolutionary calculations

We used the MESA code (Modules for Experiments in Stellar Astrophysics, Paxton et al. 2011, 2013, 2015, 2018, 2019; Jermyn et al. 2023, version 23.05.1) to construct a toy model under the non-rotating approximation. The model was created both as a product of binary interactions (through mass gain) and as a single star, allowing us to compare the binary model to its isolated counterpart. The details on variety of physical processes, which MESA relies on, can be found in Appendix A.

In our evolutionary computations, we adopted the AGSS09 (Asplund et al. 2009) initial chemical composition and used the OPAL opacity tables, supplemented by data from Ferguson et al. (2005) for lower temperatures. For high-temperature regimes, as well as hydrogen-poor or metal-rich conditions, we used CO enhanced tables. We assumed a metallicity of $Z = 0.014$ and an initial hydrogen abundance of $X_0 = 0.723$.

Convective instability in the models was treated using the Ledoux criterion, combined with the turbulent convection theory based on the Kuhfuss (1986) model, employing a mixing-length parameter of $\alpha_{MLT} = 0.5$. In regions that were stable according to the Ledoux criterion but unstable by the Schwarzschild criterion, we applied the semiconvective mixing following the formalism of Langer et al. (1985) with a scaling factor $\alpha_{sc} = 0.1$. To address regions exhibiting an inversion in the mean molecular weight, such as those formed during mass accretion, we applied the thermohaline mixing using the formalism of Kippenhahn et al. (1980), with an $\alpha_{th} = 1$ coefficient. As our models did not include rotational mixing, we introduced a minimum diffusive mixing coefficient of $D = 100 \text{ cm}^2 \text{ s}^{-1}$ to smooth out numerical noise or discontinuities in internal profiles, such as the Brunt-Väisälä frequency or composition gradients. We selected this value after testing various options, specifically $D = 10, 20, 50, 100$ and 200 , identifying it as the lowest value that effectively smoothed out numerical noise in the aforementioned profiles without erasing any significant physical structures. Additionally, we accounted for overshooting beyond the formal convective boundaries, using an overshooting parameter f_{ov} , to capture turbulent motions extending into the radiative zone. We applied an exponential scheme of Herwig (2000) on the top of the H-burning core with the value of $f_{ov} = 0.02$.

Our initial binary model consists of a $10 M_{\odot}$ donor in a 3-day circular orbit with a $7 M_{\odot}$ accretor. The initial orbital period was selected so that the donor fills its Roche lobe and initiates mass transfer while still on the main sequence. For simplicity, we assumed fully conservative mass transfer (MT), following the description of Kolb & Ritter (1990). In this scenario, the initially less massive star accretes $3 M_{\odot}$, leading to a full mass ratio reversal. Once the accretor reached $10 M_{\odot}$, all binary interactions were stopped, and we assumed that the subsequent evolution proceeded as a single star, following the standard path until central hydrogen depletion. To simulate this behaviour in MESA, we used the routine DETACH_BINARY by Mathieu Renzo¹.

For comparison purposes, we have also calculated single-star evolution for stars with masses from $7 M_{\odot}$ to $10 M_{\odot}$ with a $0.5 M_{\odot}$ step with the physics input as described above.

2.2. Pulsational calculations

To calculate pulsations using the previously described MESA models, we employed the GYRE code (Townsend & Teitler 2013; Townsend et al. 2018; Goldstein & Townsend 2020; Sun et al. 2023, version 7.1), in the adiabatic approximation. For radial pulsations ($\ell = 0$), we scanned the frequency range from 1 to 150 d^{-1} using a linear grid with 200 frequency bins. For higher mode numbers (non-radial pulsations, $\ell = 1, 2, 3, 4$), we applied an inverse grid sampling between 0.1 and 3.0 d^{-1} and a linear grid from 3.0 to 150 d^{-1} . The GYRE calculations were performed for all models in our MESA grid. These computations were applied to both single-star models and accretor models from binary evolution alike.

3. Results

3.1. Binary evolution

The early evolution of the system, initially containing $10 M_{\odot}$ and $7 M_{\odot}$ components, follows the single-star evolutionary paths, i.e. both stars detach from the Zero Age main sequence (ZAMS) and start synthesizing hydrogen in their cores. Their subsequent evolution is illustrated in the Hertzsprung–Russell (HR) diagram, in Figure 1: the donor is plotted in purple, and the accretor in gray, with both tracks overlaid on single-star reference models (dashed lines). Due to ongoing internal changes, both components start to increase their radius and move through the HR diagram at different paces. By the time the $10 M_{\odot}$ star synthesized almost all central hydrogen into helium (approximately 10% hydrogen left in the core), it has grown enough to fill its Roche lobe (at a radius of approximately $9.3 R_{\odot}$) and starts to transfer mass onto its companion (the point denoted as I_{don} in Figure 1). At this point the system is approximately 23.55 Myr old and the components begin to diverge from their single track equivalents.

As the donor star begins to transfer mass through the inner Lagrange point L_1 onto its companion during a case A mass transfer episode (Kippenhahn & Weigert 1967), it remains in thermal equilibrium. The mass transfer proceeds stably, yet rapidly, with the rate reaching up to $\dot{M} \sim 10^{-3.5} M_{\odot} \text{ yr}^{-1}$. The MT occurs on the nuclear timescale, and is primarily driven by the gradual expansion of the donor's radius resulting from internal evolutionary changes. We over plot the rate of the MT on the evolutionary tracks visible in Figure 1. As mass is transferred onto the initially less massive companion, the accretor adjusts to the increasing mass by gradually expanding in size and evolving

¹https://github.com/MESAHub/mesa-contrib/tree/release/hooks/detach_binary

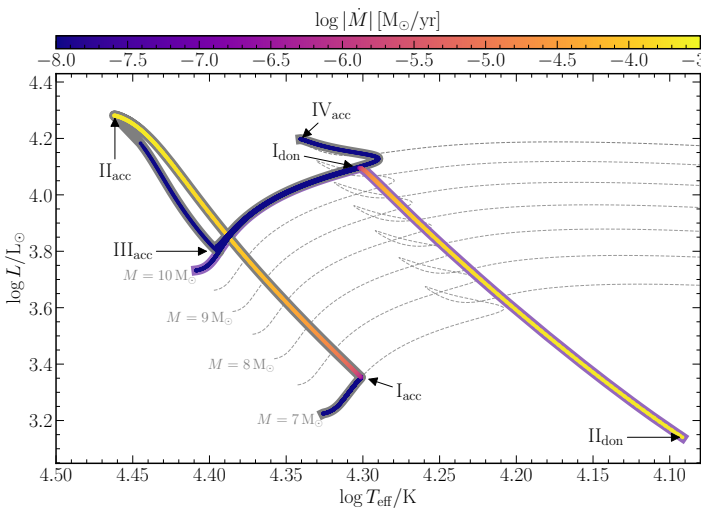


Fig. 1: The Hertzsprung–Russell diagram with the evolutionary tracks of the binary system components. The donor star is shown with purple line, and the accretor with gray line, both plotted alongside single-star reference models for different masses (dashed lines). The mass transfer/accretion rate $\log |\dot{M}|$ is over plotted along the tracks using colour coding, as indicated by the colour bar. We mark key evolutionary changes: the donor fills its Roche lobe and begins mass transfer (I_{don}), the accretor starts to gain mass and departs from its original track (I_{acc}), full mass ratio reversal when the accretor reaches $10 M_{\odot}$ and the following detachment of the system (II_{acc} and II_{don}), thermal readjustment of the accretor (III_{acc}), and the accretor’s single-star evolution until the end of the main sequence (IV_{acc}).

off its original evolutionary track (from the point denoted as I_{acc} in Figure 1). During MT, the accretor remains close to thermal equilibrium while accommodating the incoming material. As a result, it experiences a steady increase in mass, luminosity, effective temperature, and radius. We allow the accretor to grow mass until it reaches $10 M_{\odot}$, i.e. until full mass ratio reversal (the point denoted as II_{acc} in Figure 1). After this point, we artificially detach the system which allows the accretor to regain the thermal equilibrium (the point denoted as III_{acc} in Figure 1) and follow the subsequent evolution of the accretor as a single $10 M_{\odot}$ star until the the end of the main sequence phase (the point denoted as IV_{acc} in Figure 1).

3.2. General properties of the accretor model

In the mass-accreting models, the incoming mass has a severe effect on the internal structure. As the transferred material binds to the star, the induced higher central temperature boosts the nuclear energy generation rate. As the core luminosity goes up, the radiative gradient ∇_{rad} increases leading to a larger convective core region according to the convective instability criterion, as will be discussed in more detail later in this section.

The evolution of the convective core during this process is shown in Figure 2, where the core mass M_{cc} is plotted against the central hydrogen abundance X_c . For the single-star model (dashed line), the convective core steadily recedes from ZAMS to terminal age main sequence (TAMS). By contrast, the initially smaller convective core of the accretor (solid line) follows a similar trend only until $X_c \approx 0.5$, after which it expands due to mass accretion. Within just 0.02 Myr, M_{cc} increases from $1.62 M_{\odot}$ to $3.3 M_{\odot}$, reflecting the sudden influx of fresh fuel. Once mass

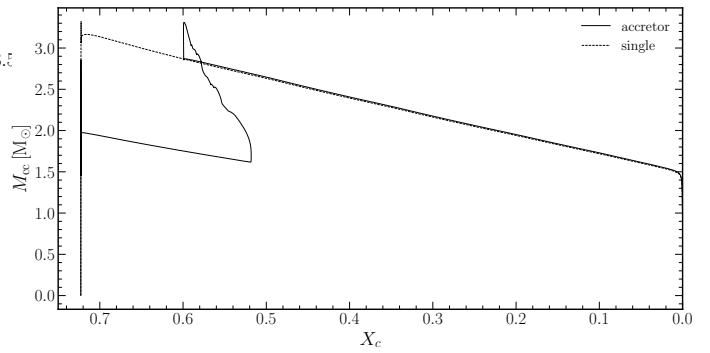


Fig. 2: The evolution of mass of the convective core M_{cc} in a function of central hydrogen abundance X_c for the single and the accretor models.

transfer ceases, the star regains thermal equilibrium and the core mass stabilizes at $M_{\text{cc}} = 2.87 M_{\odot}$ with $X_c \approx 0.6$. From that point onward, the evolution of the accretor’s convective core closely tracks that of the single-star counterpart, although it remains slightly more massive by about 1%. This offset likely results from enhanced mixing across the core-envelope boundary (CEB, Neo et al. 1977; Renzo et al. 2023), which altered the chemical profile and increased the core mass.

The structural changes brought about by accretion are clearly visible in the evolution of internal mixing and hydrogen abundance profiles, shown in Figure 3, based on the convection, overshoot, thermohaline and user-defined artificial mixing processes. The left panels show internal composition from ZAMS to TAMS, for X_c = 0.7 to 0.0, in step of 0.1. The shaded areas indicate the regions over which the mass increases, with the current mass indicated by the dashed lines. Mass accretion occurs between the second and third top panels. As the process is relatively short-lived and rapid, we present the transitional phases on the right panels, corresponding to the pre-, early-, late-, and post-Roche lobe overflow (RLOF) stages, as well as to the TAMS. The right-hand ordinates show the corresponding profiles of hydrogen abundance with black lines. These panels allow one to clearly trace the evolution of the convective core boundary in mass coordinates, both during the standard core recession and the core rejuvenation phase.

The effect of rejuvenation is twofold. As the freshly accreted material settles onto the stellar surface, an inversion in the mean molecular weight profile forms and gives rise to thermohaline mixing, which contributes to the internal redistribution of chemically stratified layers (Kippenhahn et al. 1980; Wagg et al. 2024). The expansion of the convective core during accretion leads to the engulfment of previously receding layers, mixing hydrogen-rich material from the envelope into the core (Neo et al. 1977). At the same time, this process compresses the surrounding chemically stratified region, steepening the hydrogen gradient in the adjacent layers. As a result, the mean molecular weight μ drops sharply in this narrow zone, and an inflection in the density profile emerges. Specifically, a slightly increased density in the location of the previously engulfed regions is followed by a steeper decline due to drop in μ , compared to the single models as shown in Figure 4. We refer to this feature as a local bump in the density profile. This bump reflects a deviation from the otherwise monotonic density gradient and emerges just above the growing convective core, in layers enriched in hydrogen as a signature of structural reconfiguration due to accretion. As the core expands during the mass accretion, it shifts this kink

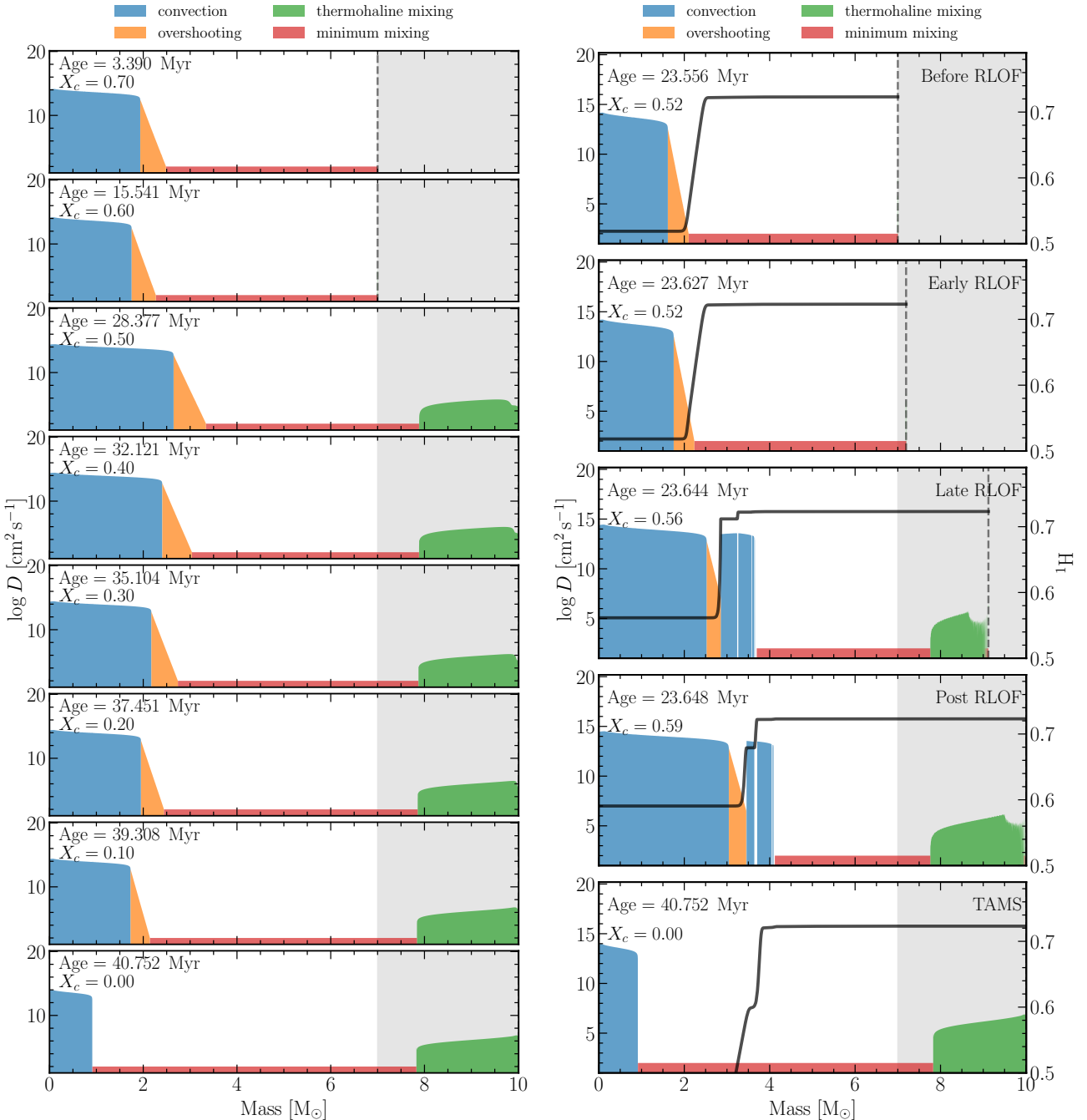


Fig. 3: The mixing profiles D during the evolution of the accretor. Left: Evolution from $X_c = 0.7$ to 0.0 in steps of 0.1. Right: Profiles at selected evolutionary stages, before, during and after the RLOF. The shaded areas indicate the regions over which the mass varies, with the current mass indicated by dashed lines. The black lines, as denoted on the right-hand ordinates of the right panels show the corresponding profiles of hydrogen abundances.

into higher layers, near the end of the hydrogen gradient region. This feature is stable, meaning that it persists at least until the end of the main sequence phase (see Figure 4). The presence of this bump is also consistent with earlier findings by Renzo et al. (2023) and Wagg et al. (2024), though the models of the former authors describe a local *dip* in the density profile.

A key consequence of the density bump is the development of off-centre convective zones (oCZs). These zones appear in the chemically stratified region above the convective core during the late and post-RLOF phases, as seen in the right panels of Figure 3. Their occurrence has been reported by Renzo & Götberg

(2021) and their physical origin was analysed by Miszuda (submitted to A&AL). The formation of oCZs is governed by the Ledoux criterion for convective instability. According to this condition, a region becomes unstable to convection if the actual temperature gradient exceeds the Ledoux gradient

$$\nabla > \nabla_L = \nabla_{\text{ad}} + \frac{\varphi}{\delta} \nabla_\mu, \quad (1)$$

where ∇ is the temperature gradient, ∇_{ad} is the adiabatic temperature gradient, and ∇_μ is the gradient of the mean molecular

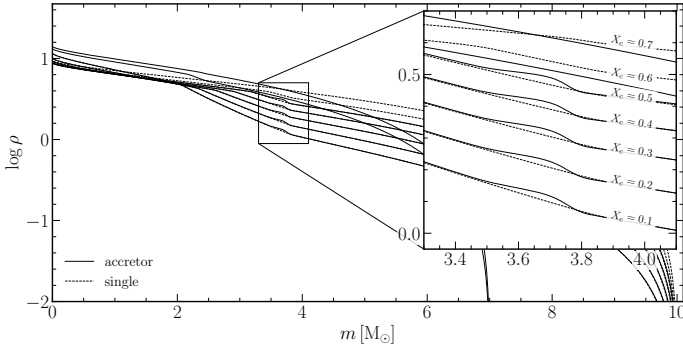


Fig. 4: The density $\log \rho$ profiles at selected central hydrogen abundances X_c , for the single-star (dashed lines) and the accretor (solid lines) models. The local bump discussed in the text is clearly visible in the binary models.

weight:

$$\nabla = \frac{d \ln T}{d \ln P}, \quad \nabla_{ad} = \left(\frac{\partial \ln T}{\partial \ln P} \right)_{ad} \quad \text{and} \quad \nabla_{\mu} = \frac{d \ln \mu}{d \ln P}. \quad (2)$$

The thermodynamic derivatives

$$\delta = - \left(\frac{\partial \ln \rho}{\partial \ln T} \right)_{P,\mu} \quad \text{and} \quad \varphi = \left(\frac{\partial \ln \rho}{\partial \ln \mu} \right)_{P,T} \quad (3)$$

are obtained from the equation of state (e.g., Kippenhahn & Weigert 1990). In radiative layers, where energy is transported by radiation, the actual temperature gradient ∇ is equal to the radiative temperature gradient ∇_{rad} . Therefore, in these layers, the Ledoux instability criterion takes the form of

$$\nabla_{rad} > \nabla_L. \quad (4)$$

In the post-mass transfer models, the appearance of a local density bump leads to an increase in opacity, which enhances ∇_{rad} . If this exceeds the stabilising contribution from ∇_{μ} , the stability Ledoux criterion is violated and a convective zone forms away from the centre — giving rise to the oCZ.

The oCZs play a critical role in reshaping the hydrogen abundance profile. As they develop within chemically stratified zones, they homogenize the local composition by erasing sharp gradients. The mixing within the oCZ reduces the mean molecular weight gradient leading to flat regions in hydrogen followed by new discontinuities at the oCZ boundaries. These discontinuities increase ∇_L and can suppress convection locally, effectively splitting or terminating the oCZs. At the same time, the chemically stratified region continues to be compressed by the outward growth of the convective core during the rejuvenation. This compression can again steepen ∇_{rad} , allowing it to exceed ∇_L and temporarily revive convection. During the mass transfer episode, multiple density bumps form at the boundaries of successive oCZs (Miszuda, submitted to A&AL) altering the hydrogen abundance profiles. However, only the final feature, formed just before the disappearance of the last oCZ at the end of the mass-accretion phase, persists into the post-mass transfer phases. Because it forms sufficiently far from the convective core, it is not smoothed-out by overshooting and thus remains as a lasting structural relic of the accretion history. The impact of this feature on the chemical structure is illustrated in Figure 5, where we compare hydrogen abundance profiles at various evolutionary phases between the single-star (dashed lines) and accretor

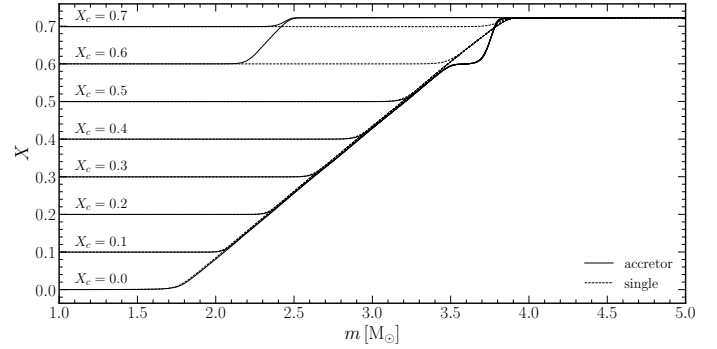


Fig. 5: Hydrogen abundances X in a function of a mass for different evolutionary stages of $10 M_{\odot}$ single (dashed lines) and accretor (solid lines) models. For clarity, we only show the fraction of the inner mass coordinate.

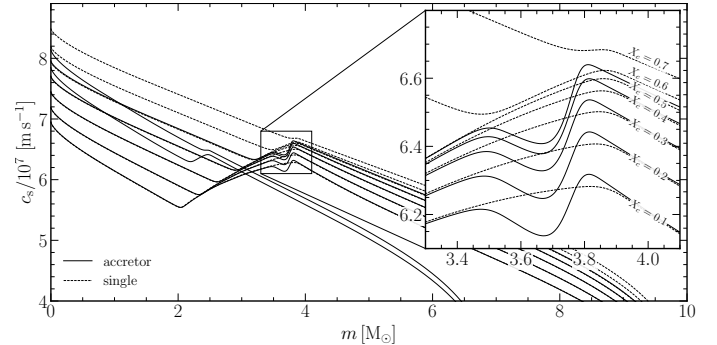


Fig. 6: The sound speed c_s profiles at selected central hydrogen abundances X_c , for the single-star (dashed lines) and the accretor (solid lines) models.

(solid lines) models. This abundance kink remains clearly visible for $X_c \leq 0.5$, for $3.5 < m / M_{\odot} < 3.8$, highlighting its persistence throughout the post-mass transfer main sequence evolution.

The structural imprint of the density bump is also reflected in the sound-speed profile. Since the adiabatic sound speed is defined as

$$c_s^2 = \Gamma_1 P / \rho, \quad (5)$$

where Γ_1 is the first adiabatic exponent, P is the pressure and ρ is the density, hence any local modulation in the density at fixed pressure alters the sound speed. In the region near the CEB, where pressure gradients are smooth due to hydrostatic equilibrium, the density bump causes a clear deviation in the c_s profile, as shown in Figure 6. This modulation has observable consequences, as it affects the propagation of p modes and may alter mode trapping behaviour (e.g., Dziembowski et al. 1993; Miglio et al. 2008). We investigate these effects in more detail in the following sections.

3.3. Asteroseismic properties of the accretor model

There are two characteristic frequencies that determine the behaviour of stellar oscillations. These are the Lamb frequency:

$$S_{\ell}^2 = \frac{\ell(\ell+1)c_s^2}{r^2}, \quad (6)$$

and the Brunt-Väisälä frequency:

$$N^2 = g \left(\frac{1}{\Gamma_1 P} \frac{dP}{dr} - \frac{1}{\rho} \frac{d\rho}{dr} \right) \quad (7)$$

(e.g., Aerts et al. 2010). Here, ℓ is the spherical harmonic degree, c_s is the adiabatic speed of sound, g is the local gravitational acceleration and r is the radial coordinate.

The propagation of modes is determined by the relation between the oscillation frequency ω and the characteristic frequencies N and S_ℓ ². Modes for which $|\omega| < |N|$ and $|\omega| < |S_\ell|$ propagate as gravity modes (g modes), for which buoyancy acts as the restoring force. They are confined to radiative zones, where $N^2 > 0$, while convective zones act as evanescent barriers (e.g., Cox 1980; Aerts et al. 2010). In chemically homogeneous, non-rotating and non-magnetic stars, the g modes with consecutive radial orders n and the same spherical degree ℓ exhibit equally spaced periods ΔP . According to the asymptotic properties of g modes, valid for $\ell \ll n$, this spacing remains constant and is given by (Tassoul 1980):

$$\Delta P_{\ell,\text{asym}} = \frac{2\pi^2}{\sqrt{\ell(\ell+1)}} \left(\int_C N r^{-1} dr \right)^{-1}, \quad (8)$$

where the integration is performed over the g mode propagation cavity C with respect to the radial coordinate. This expression shows that the period spacing is determined by the integral of the Brunt-Väisälä frequency, and is therefore highly sensitive to the presence of chemical gradients and sharp structural features in the deep interior of the star. In case of the main sequence massive stars, with convective core and radiative envelope, the observed value of ΔP is directly related to the extent of the core (e.g., Moravveji et al. 2015, 2016; Mombarg et al. 2019; Pedersen et al. 2018, 2021).

In contrast, modes with $|\omega| > |N|$ and $|\omega| > |S_\ell|$ propagate as pressure modes (p modes), for which pressure acts as the restoring force. These propagate in the outer layers, where the sound speed and density is lower and the acoustic cavity is located. In massive main sequence stars like β Cephei variables, only low- to intermediate-order p modes are observed. These modes of moderate radial order can penetrate into the deep stellar interior, making them valuable probes of the region near the convective core. Because of this dependence, p mode frequencies can provide a complementary asteroseismic diagnostic to g mode periods, especially in stars that have undergone structural changes due to processes such as mass accretion. Changes in the internal c_s profile, for instance due to convective core expansion, envelope compression, or compositional readjustment, can subtly shift the p mode frequencies and thus leave observable signatures in the mode spectrum.

3.3.1. The Brunt-Väisälä frequency

The study of the Brunt-Väisälä frequency N profile is essential to understand how mass accretion modifies the internal structure of massive stars. In particular, it allows us to trace the chemical and thermal stratification that governs the propagation of buoyancy modes within a star. Following the ideal gas law for a fully ionised gas approximation, N can be expressed as (e.g., Cox 1980; Brassard et al. 1991; Miglio et al. 2008):

$$N^2 \approx \frac{g^2 \rho}{P} (\nabla_{\text{ad}} - \nabla + \nabla_\mu). \quad (9)$$

The chemical gradient ∇_μ is extremely important in asteroseismology of massive stars with convective cores. As the star evolves on the main sequence, the fully mixed core shrinks leaving a gradient of hydrogen (see Figure 5) and helium abundance.

This causes a positive contribution to the ∇_μ and hence, causing an emergent rise of N (Kippenhahn & Weigert 1990). As the star evolves and the convective core recedes, the peak extends to the deeper parts of the star in a transition region adjacent to the core. The chemical gradient acts stabilising on the convection (Ledoux 1947), and thus this region defines a boundary for the g mode cavity as the trapping occurs in the μ gradient zone (Dziembowski et al. 1993).

By expansion of the convective core, the presence of the oCZs produce a deviation from the otherwise monotonic increase in hydrogen profile (see Figure 5, solid lines) in the form of a plateau followed by an additional steep chemical gradient close to the outer boundary of the main chemical stratification. That gradient causes additional contribution to ∇_μ (see top panels of Figure 7) and thus to N (see lower panels of Figure 7) producing the bimodal distribution. As the star progresses through the main sequence, that feature persists, at least until TAMS, after which the star restructures its interior and develops a deep convective zone, that potentially can wash out this effect. The stability of the bimodal structure in N across various evolutionary stages is visible in Figure 7.

3.3.2. g modes

The presence of two distinct peaks in N profile leads to the trapping of specific modes within specific stellar regions, thereby modifying their periods and inducing deviations from the asymptotic period spacing (e.g., Dziembowski et al. 1993; Miglio et al. 2008). These effects have been recently explored by Wagg et al. (2024) and Henneco et al. (2025) for intermediate-mass SPB pulsator and massive merger models, respectively. We revisit them here, as we see a similar behaviour for the g modes.

As the accretor evolves on the early main sequence, the period spacing closely follows the asymptotic value. However, once the convective core begins to recede and a chemical gradient forms at its boundary, the $\Delta P(P)$ pattern develops regular oscillations around the asymptotic value, typically within a $P \sim 1$ day range. During the mass transfer episode, the spacing pattern becomes increasingly irregular, with no clear periodicity or coherence. This behaviour reflects rapid structural changes, the emergence of the off-centre convective zones, and the development of a highly structured Brunt-Väisälä profile shaped by composition gradients and complex mixing. In the final stages of the main sequence, the period spacing pattern stabilises and regains regularity with a modulated oscillatory behaviour, and the amplitude alternating between increasing and decreasing in a quasi-periodic manner. The amplitude varies in a cyclic fashion, resembling a beating pattern. This behaviour likely results from mode trapping between multiple internal layers, shaped by persistent chemical gradients near the convective core boundary, and reflects the increasingly stratified structure of the stellar interior as the star approaches the terminal age main sequence. Such a behaviour can be seen in Figure 8, in which we plot the dipole mode period spacing ΔP for the accretor and single star models, corresponding to four separate evolutionary cases: pre-MT case at $X_c = 0.7$, and post-MT at $X_c = 0.5, 0.3$ and 0.1 . With horizontal lines, we mark the asymptotic ΔP values (see Equation 8), using solid lines for the accretor model and dashed lines for the equivalent single model. At $X_c = 0.7$, both models exhibit nearly constant period spacings, with almost all modes lying close to the asymptotic value. This indicates a very small chemical composition gradient. Additionally, due to different initial masses, the asymptotic values themselves differ between the models, reflecting the dependence of the Brunt-Väisälä integral on the stel-

²Here, presented in an angular form.

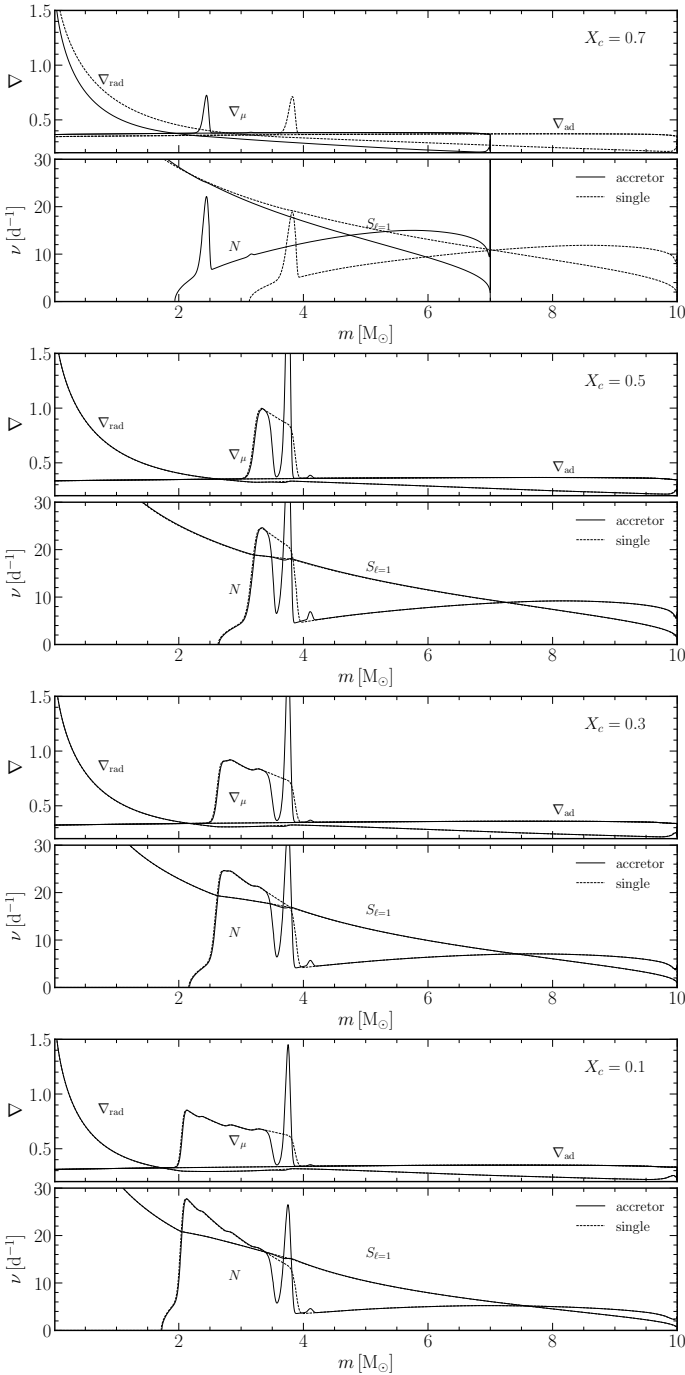


Fig. 7: The variation of radiative ∇_{rad} , adiabatic ∇_{ad} and chemical ∇_{μ} gradients (the top panels) along with Lamb $S_{\ell=1}$ and Brunt-Väisälä N frequencies (the bottom panels) in a function of mass for $10 M_{\odot}$ single (dashed lines) and accretor (solid lines) models. We show results at four different evolutionary stages, $X_c = 0.7, 0.5, 0.3$ and 0.1 .

lar size and internal structure. As evolution proceeds, after the mass transfer and mass equalization, the period spacing patterns begin to overlap, yet subtle differences persist between the models. Characteristic dips in the period spacing diagram start to emerge, associated with the development of a μ gradient region just outside the convective core. These dips are caused by mode trapping and result from the local increase in the Brunt-Väisälä frequency. Their presence and depth provide valuable asteroseis-

mic diagnostics of the internal chemical stratification and the evolutionary state.

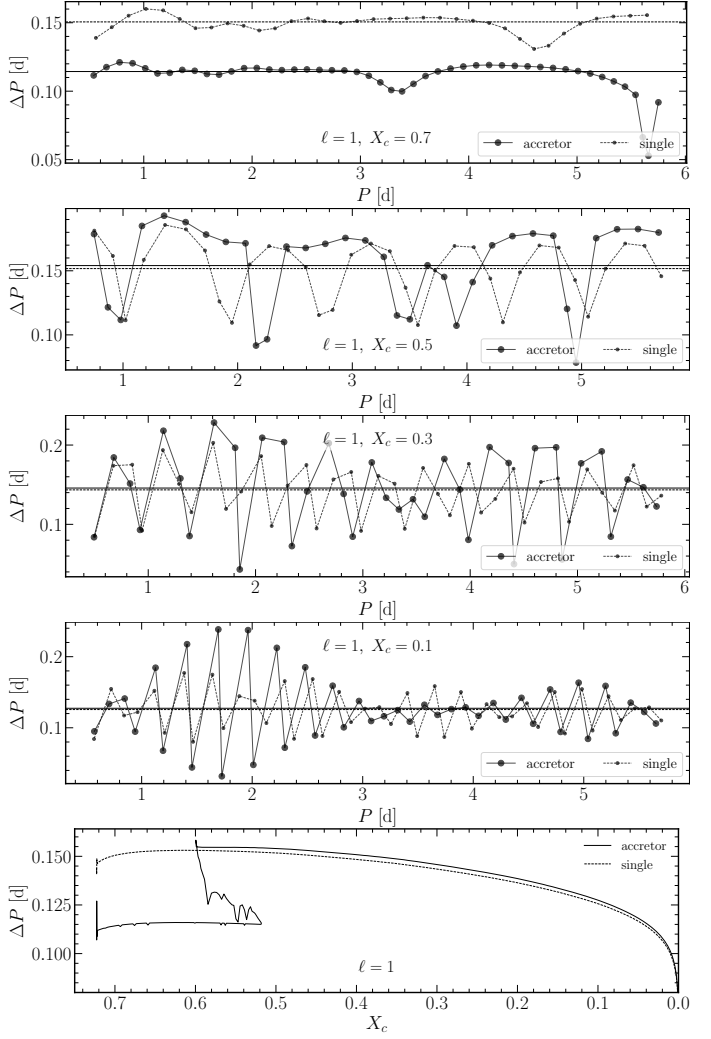


Fig. 8: The period spacing diagrams showing dipole g modes, for both the accretor model (solid line) and the single-star model (dotted line). The horizontal lines mark the asymptotic value of the period spacing. We show results for only four different evolutionary stages, $X_c = 0.7, 0.5, 0.3$ and 0.1 . The bottom panel shows the comparison of evolution of asymptotic value of the period spacing between the accretor and the single model.

At the bottom panel of Figure 8, we also show the evolution of the asymptotic ΔP values as a function of central hydrogen abundance X_c . For the accretor model, ΔP remains nearly constant at $\Delta P \sim 0.115$ d from the ZAMS up to $X_c \approx 0.5$. Following the onset of mass accretion, ΔP increases rapidly, reaching a peak value of $\Delta P \sim 0.16$ d at $X_c \approx 0.6$ and later stabilizes at $\Delta P \sim 0.155$ d. After mass transfer ends, the accretor evolves similarly to the single-star model, but with asymptotic ΔP values consistently higher by about 2%. This offset can be linked directly to changes in the Brunt-Väisälä frequency profile induced by mass accretion and structural readjustment.

We confirm the findings of Wagg et al. (2024), that the period spacing pattern has a larger amplitude for the accretor compared to the single-star models. Additionally, for specific periods, the accretor's pattern can be out of phase with the single star's. This may be the most evident for $X_c = 0.1$, in the second-to-last panel of Figure 8. The observed changes in period spacings be-

Mode frequency	Accretor model [d ⁻¹]	Single model [d ⁻¹]	Frequency ratio
$\nu_{\ell=1,n=2}$	5.2558	5.2866	0.9942
$\nu_{\ell=1,n=3}$	5.9026	5.9385	0.9940
$\nu_{\ell=2,n=1}$	5.6151	5.6261	0.9980
$\nu_{\ell=2,n=7}$	11.4773	11.5289	0.9955
$\nu_{\ell=3,n=2}$	7.3094	7.3372	0.9962
$\nu_{\ell=3,n=9}$	13.8466	13.9073	0.9956
$\nu_{\ell=4,n=0}$	5.8409	5.7469	1.0164
$\nu_{\ell=4,n=3}$	8.7445	8.7952	0.9942
$\nu_{\ell=4,n=10}$	15.3680	15.4295	0.9960

Table 1: A comparison between accretor and single-star frequencies for a given modes, corresponding to $X_c = 0.1$ evolutionary stage.

tween the accreting and single-star models indicate that mass transfer leaves detectable asteroseismic signatures. The magnitude of these differences, particularly in the g mode regime, suggests that they could be within the observational capabilities of missions such as *Kepler* (Koch et al. 2010), *TESS* (Ricker et al. 2015) or their successors, such as *PLATO* (Rauer et al. 2014), provided that a sufficient number of consecutive modes can be identified.

3.3.3. p modes

In the case of p modes, we are primarily interested in low-degree, low to medium-order modes, since they are most likely to probe the deeper parts of the stellar interiors. For such modes, we calculate the accretor to single star frequency ratio $\nu_{\ell,n_{pg}}^{\text{acc}} / \nu_{\ell,n_{pg}}^{\text{sin}}$ for equal degree and order. We present the result in Figure 9 for four separate evolutionary cases, $X_c = 0.7, 0.5, 0.3$ and 0.1 . Similarly as in Figure 8, the top panel shows the pre-MT case, where we have a mismatch between the stellar masses. However, as shown in the following panels, distinct deviations between accretor and single star frequencies appear in the low- to intermediate-order regime. These are superimposed on a systematic offset observed in the asymptotic region, where the frequency ratio $\nu_{\ell,n_{pg}}^{\text{acc}} / \nu_{\ell,n_{pg}}^{\text{sin}}$ reaches approximately 1.0012 for $X_c = 0.5$, 0.996 for $X_c = 0.3$, and 0.9925 for $X_c = 0.1$. To illustrate this in more detail, we select the representative model at $X_c = 0.1$ and list the corresponding frequencies and their exact ratios in Table 1. As can be seen, the most affected frequencies are in $5 - 15$ d⁻¹ range, which is the typical observed range for β Cep stars (eg., Stankov & Handler 2005). These non-asymptotic p modes are more sensitive to conditions in the near-core region, including the sound-speed gradient and the local stratification shaped by previous mass accretion. As a result, their frequency deviations provide direct seismic evidence of internal restructuring. In order to quantify this sensitivity and link the frequency shifts to structural differences, we compute the weight functions. These allow us to identify the specific layers where the eigenfunctions contribute most significantly to the observed frequency deviations.

It was shown by Kawaler et al. (1985) and later revised by Townsend & Kawaler (2023) that the variational expression for the eigenfrequency of a mode can be written as

$$\sigma^2(\mathbf{y}) = \frac{\int_0^R [C(\mathbf{y}, r) + N(\mathbf{y}, r) + G(\mathbf{y}, r)] \rho r^2 dr}{\int_0^R T(\mathbf{y}, r) \rho r^2 dr}, \quad (10)$$

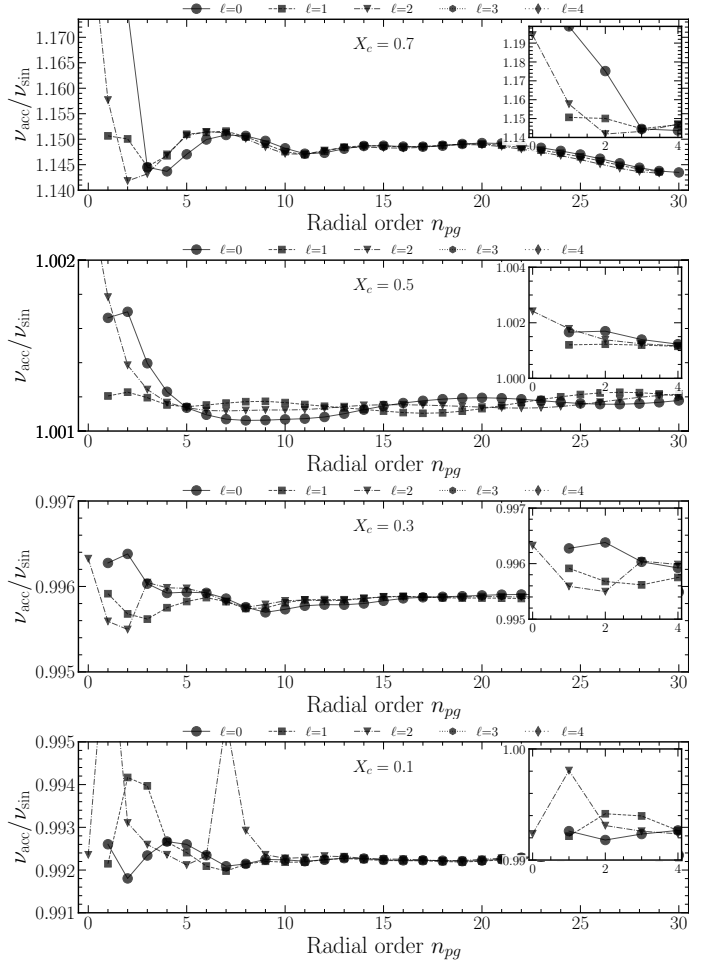


Fig. 9: The accretor and single-star frequency ratios for a given modes at different evolutionary stages, $X_c = 0.7, 0.5, 0.3$ and 0.1 .

where

$$C(\mathbf{y}, r) = g^2 \ell(\ell + 1) S_\ell^{-2} (y_2 - y_3)^2, \quad (11)$$

$$N(\mathbf{y}, r) = r^2 N^2 y_1^2, \quad (12)$$

$$G(\mathbf{y}, r) = -\frac{gr}{U} [y_4 + (\ell + 1)y_3]^2 \quad (13)$$

are weight functions and $\mathbf{y}(r) = \{y_1(r), y_2(r), y_3(r), y_4(r)\}$ is a vector of eigenfunctions introduced by Dziembowski (1971), corresponding to the radial displacement, the Eulerian pressure perturbation, the gravitational potential perturbation and its derivative. Weight functions highlight the internal regions of the star that contribute to the mode's frequency, revealing its sensitivity to specific layers and hence establishing its main formation regions. These have been used extensively to examine the mode trapping properties in subdwarf B (sdB) stars (Charpinet et al. 2000; Guyot et al. 2025).

The function in the denominator,

$$T(\mathbf{y}, r) = r^2 \left[y_1^2 + \ell(\ell + 1) \left(\frac{q}{r\sigma^2} \right)^2 y_2^2 \right], \quad (14)$$

is proportional to the kinetic energy density and the U quantity, appearing in Equation 13, is the homology invariant (see eg., Kippenhahn & Weigert 1990).

The frequency of a given mode $\nu_{\ell,n}$ can be expressed as

$$\nu_{\ell,n}^2 = V(x = 1), \quad (15)$$

where V is a cumulative integral of the weight functions W over a normalised radius $x = r/R$,

$$V(x) = \int_0^x W(x') dx'. \quad (16)$$

This is connected with [Equation 10](#) via

$$\nu = V(1)^{1/2} = \left(\frac{GM}{R^3}\right)^{1/2} \left(\frac{86\,400}{2\pi}\right)^{-1} \sigma. \quad (17)$$

We calculate the weight functions W for the modes that show the largest frequency deviation between the two models at $X_c = 0.1$, specifically those with $(\ell, n) = (1, 2), (1, 3), (2, 1), (2, 7), (3, 2), (3, 9), (4, 0), (4, 3)$, and $(4, 10)$ (see [Figure 9](#) and [Table 1](#)). These weight functions are shown in [Figure 10](#), together with their cumulative integrals V . The insets zoom into the region $0.07 < r/R_{\odot} < 0.15$ (corresponding to $1 < m/M_{\odot} < 4.5$). The differences $\Delta W = W_{\text{accretor}} - W_{\text{single}}$ and $\Delta V = V_{\text{accretor}} - V_{\text{single}}$ are shown as grey dashed lines, plotted on the right-hand y-axes of the top and bottom panels, respectively.

The analysis of p mode frequency ratios further confirms that mass accretion subtly but measurably alters the sound-speed profile of the star. These variations, although smaller than those observed in the g mode period spacings, offer complementary diagnostics sensitive to the layers close to the core and can thus provide additional constraints in asteroseismic modelling of mass-accreting systems. In particular, the differences in weight functions ΔW and the cumulative integrals ΔV indicate that the dominant contribution to the frequency shifts originates from the region $0 < m/M_{\odot} < 4$, which coincides with the zone of strongest divergence in the sound-speed profiles c_s between the accretor and the single-star model (see [Figure 6](#)). This region encompasses the outer edge of the convective core and adjacent stratified layers shaped by the accretion history. The frequency deviations can thus be interpreted as a seismic signature of the structural imprint left by the mass transfer event. The magnitude of these frequency shifts, typically of the order of 0.5%, corresponds to absolute differences of $\sim 0.03 - 0.07 \text{ d}^{-1}$, in the $5 - 15 \text{ d}^{-1}$ range. These are well above the typical observational uncertainties for β Cep stars ($\sim 0.003\%$, e.g., [Jerzykiewicz et al. 2005](#); [Bursse et al. 2023](#)), and are therefore very likely to be detectable.

3.3.4. High-order p modes

Even though high-order p modes are not observed in β Cephei pulsators, we explore the asymptotic properties of the p modes, as their asymptotic behaviour might offer a valuable theoretical framework for comparison.

It is well known that a local glitch such as a discontinuity in sound speed or density can induce periodic variations in the p mode frequencies ([Gough 1990](#)). For solar-like oscillators, the bottom of convective envelop and the partial ionization zone of helium, have been inferred from high-frequency p modes ([Roxburgh & Vorontsov 1994](#); [Basu et al. 1994](#)). The observables include the small frequency separation $\delta_{02} = \nu_{n,\ell} - \nu_{n-1,\ell+2}$ or the second-order frequency differences $\nu_{n-1,l} - 2\nu_{n,l} + \nu_{n+1,l}$ ([White et al. 2011](#); [Verma et al. 2014](#)).

From the asymptotic analysis, the small separation over large separation ratio $\delta_{02}/\Delta\nu$ can be approximated as

$$\delta_{02}/\Delta\nu \approx \frac{(2\ell + 3)}{4\pi^2\nu} \left(- \int \frac{dc}{dr} \frac{dr}{c} + \frac{c(R)}{R} \right). \quad (18)$$

Thus, the imprints of mass transfer on the sound speed gradient near the core directly affect the magnitude of small separation. The above approximation has been refined and applied to red giants recently by [Ong et al. \(2025\)](#) and [Reyes et al. \(2025\)](#).

[Figure 11](#) presents the ratio of the small to large frequency separations, computed using GYRE (black lines) and from the leading-order asymptotic approximation (gray lines) for both the accretor and single-star models. As expected from theory, the asymptotic estimate of $\delta\nu_{02}/\Delta\nu$ decreases monotonically with increasing radial order n_{pg} , a trend that aligns well with the GYRE calculations in the high-order regime. Notably, the accretor model exhibits a slightly small to larger separation ratio compared to the single-star model. This difference can be attributed to a larger integral of the sound-speed gradient in the accretor model (see [Equation 18](#)). Superimposed on the overall decline is a periodic modulation, which arises from the density discontinuity of the convective core boundary.

Following [Roxburgh & Vorontsov \(1994\)](#), the amplitude of this variation depends on the magnitude of the density discontinuity, and the period of the variational component can be approximated by

$$\tilde{P} = (T/t_{\text{core}})\Delta\nu, \quad (19)$$

where t is the acoustic radius

$$t(r) = \int_0^r \frac{dr}{c}, \quad (20)$$

and $T = t(r = R)$, $t_{\text{core}} = t(r = r_{\text{core}})$. Since the large frequency separation is given by $\Delta\nu \approx 1/(2T)$, we can estimate the frequency of the variation as

$$\tilde{f} = 1/\tilde{P} = 2t_{\text{core}}. \quad (21)$$

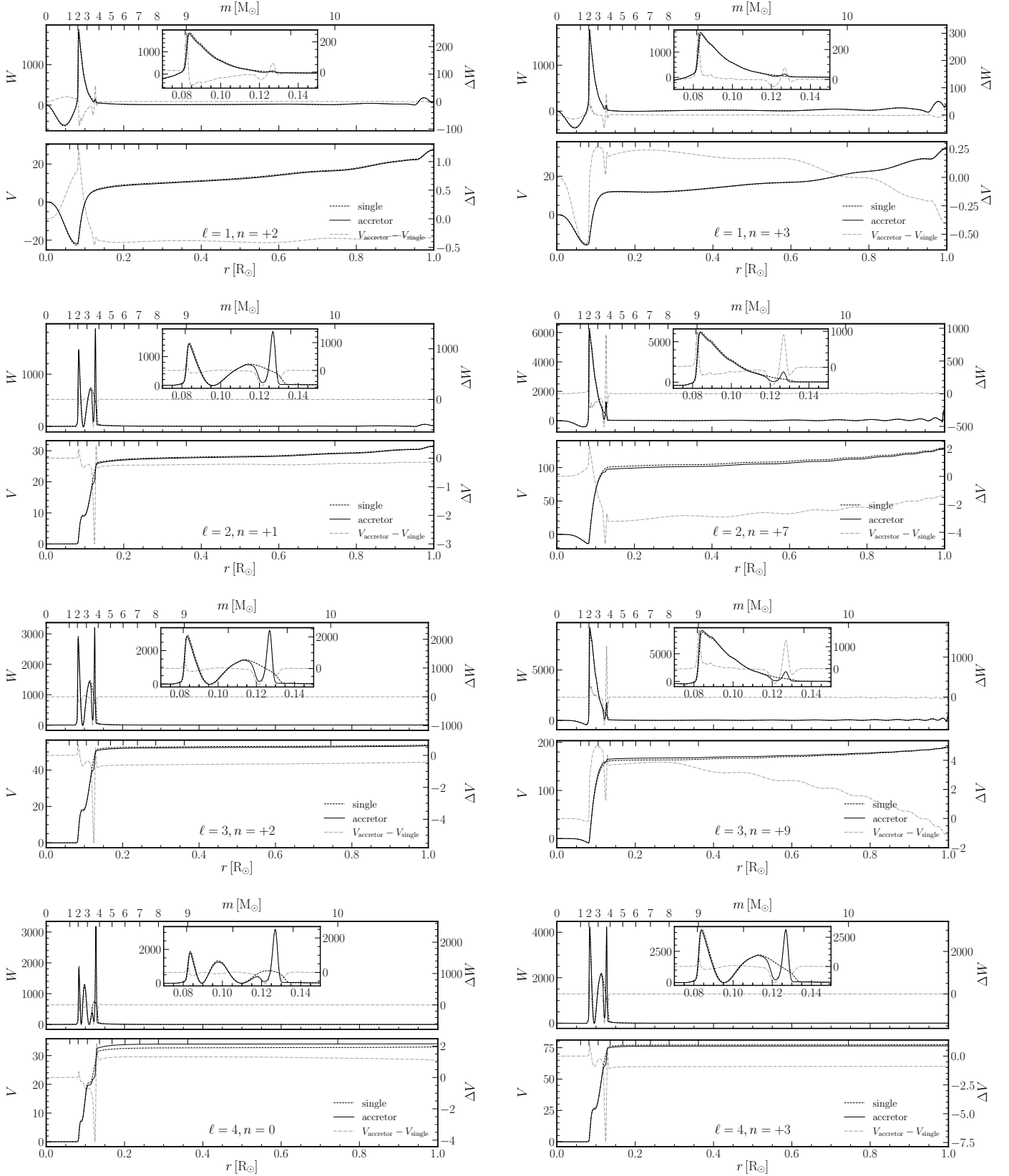
We measure the periodic component in $\delta\nu_{02}/\Delta\nu$ by recording the local minima and calculating the averaged period from high radial order p modes from GYRE ($n_{\text{pg}} > 30$) and find nice agreement with the expected frequency $2t_{\text{core}}$. We note that $\delta\nu_{02}/\Delta\nu$ of the accretor model (solid lines) has a slightly larger period than that of the single model (dashed lines), indicating a larger T/t_{core} ratio.

These results highlight the sensitivity of high-order p modes to structural discontinuities introduced by mass transfer, and demonstrate how asymptotic diagnostics, even if not directly observable in β Cephei stars, can provide valuable insights into the internal structure of post-interaction models.

4. Summary

In this study, we investigate the structural and asteroseismic consequences of mass accretion onto a main sequence star with a final mass of $10 M_{\odot}$, representative of a typical β Cephei pulsator. We compare a single-star model and an accretor model that has undergone conservative mass transfer, focusing on key internal diagnostics such as density, chemical composition, sound speed, Brunt-Väisälä frequency and g mode and low-order p mode frequencies.

Mass accretion significantly modifies the internal structure and asteroseismic properties of the β Cep accretor. The most prominent structural change is the formation of a local bump in the density profile just above the convective core. This feature arises during rejuvenation when the core expands and engulfs hydrogen-rich layers, creating a sharp μ gradient and a non-monotonic density kink. The bump persists throughout the main



sequence evolution and corresponds to a lasting chemical discontinuity visible at the outer-boundary of the μ gradient region.

These structural modifications are reflected in the Brunt-Väisälä frequency profiles. While the single-star model shows a smooth Brunt-Väisälä profile shaped solely by core retreat and

composition gradients, the accretor exhibits a bi-modal profile that results in additional mode trapping.

The g mode period spacing diagram offers a sensitive asteroseismic probe of these structural changes. Before accretion, both models show near-constant ΔP values, closely matching the

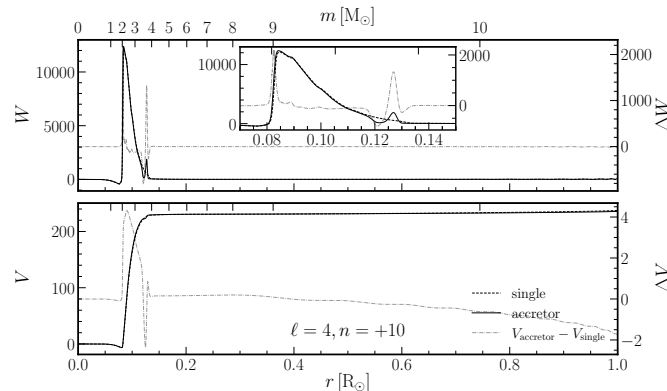


Fig. 10: Weight functions W and their cumulative integrals V for the specific modes listed in Table 1 at $X_c = 0.1$, showing most distinct deviations between accretor and single-star frequencies.

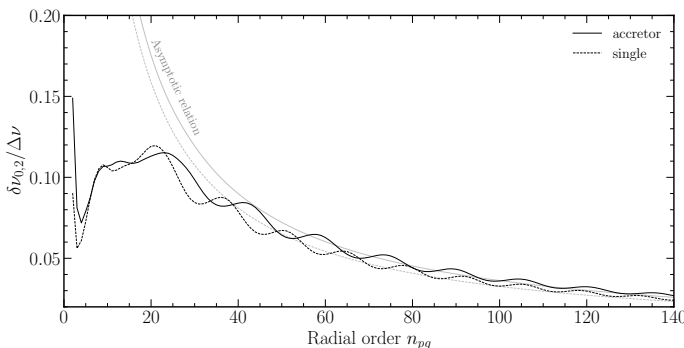


Fig. 11: The ratio of the small frequency separation $\delta\nu_{02}$ derived from $\ell = 0$ and $\ell = 2$ p modes, to the large frequency separation $\Delta\nu$, is shown as a function of radial order. The asymptotic values are represented by smooth grey lines, while the black lines correspond to the results obtained from GYRE. Both the single-star and the accretor models are included for comparison.

asymptotic expectation. However, during and after mass transfer, the period spacing of the accretor becomes irregular due to rapid internal restructuring. Once the star reaches post-accretion state, ΔP patterns regain coherence but develop characteristic modulations. These features result from mode trapping in the layered structure around the convective core and trace the evolving composition gradients. The quasi-periodic modulations in period spacing, including beating-like behaviour, serve as direct signatures of internal stratification shaped by mass accretion.

Low- and intermediate-order p modes are likewise affected. Frequency ratios $\nu^{\text{acc}}/\nu^{\text{sin}}$ reveal systematic shifts up to $\sim 0.5\%$, corresponding to absolute differences of $0.03 - 0.07 \text{ d}^{-1}$ in the observable $5 - 15 \text{ d}^{-1}$ range for β Cephei stars. These shifts arise primarily from differences in the sound-speed profile near the core due to the local density bump. Weight function analysis confirms that these layers dominate the contribution to the observed frequency deviations.

Finally, we detect changes in the $\delta\nu_{02}/\Delta\nu$ patterns. The accretor shows a slightly longer modulation period, indicating a larger T/t_{core} ratio. This further confirms the seismic signature of a structurally more extended core boundary region caused by prior mass accretion.

In summary, we demonstrate that mass accretion leaves measurable imprints on the internal structure of mass-accreting stars, especially in density, chemical gradients, and sound-speed pro-

files. These translate into observable differences in both g and p mode pulsations. Period spacing modulations, mode trapping features, and systematic frequency shifts provide robust asteroseismic diagnostics of prior mass transfer events. Such signatures are within the sensitivity of current high-precision photometry, making asteroseismology a powerful tool to probe the evolutionary history of massive stars in binary systems.

Appendix A: **MESA** input physics

The MESA code builds upon the efforts of many researchers who advanced our understanding of physics and relies on a variety of input microphysics data. The MESA EOS is a blend of the OPAL (Rogers & Nayfonov 2002), SCVH (Saumon et al. 1995), FreeEOS (Irwin 2004), HELM (Timmes & Swesty 2000), and PC (Potekhin & Chabrier 2010) EOSes. Radiative opacities are primarily from the OPAL project (Iglesias & Rogers 1993, 1996), with data for lower temperatures from Ferguson et al. (2005) and data for high temperatures, dominated by Compton-scattering from Buchler & Yueh (1976). Electron conduction opacities are from Cassisi et al. (2007). Nuclear reaction rates are from JINA REACLIB (Cyburt et al. 2010) plus additional tabulated weak reaction rates from Fuller et al. (1985), Oda et al. (1994) and Langanke & Martínez-Pinedo (2000). Screening is included via the prescription of Chugunov et al. (2007). Thermal neutrino loss rates are from Itoh et al. (1996). The MESA-BINARY module allows for the construction of a binary model and the simultaneous evolution of its components, taking into account several important interactions between them. In particular, this module incorporates angular momentum evolution due to mass transfer. Roche lobe radii in binary systems are computed using the fit of Eggleton (1983). mass transfer rates in Roche lobe overflowing binary systems are determined following the prescriptions of Ritter (1988) and Kolb & Ritter (1990).

Appendix B: **MESA** inlists

```

! inlist_project
&binary_job
  inlist_names(1) = 'inlist1'
  inlist_names(2) = 'inlist2'

  evolve_both_stars = .true.
/ ! end of binary_job namelist

&binary_controls
  photo_digits = 5

  m1 = 10.0
  m2 = 7.0
  initial_period_in_days = 3.0
  mdot_scheme = "Kolb"

  terminate_if_L2_overflow = .true.

  mass_transfer_beta = 0.0

  ! timestep controls
  fa = 0.02d0
  fa_hard = 0.05d0
  fr = 0.01
  fr_limit = 2.5d-2
  fr_dt_limit = 500
  fm = 1d0
  fm_limit = 1d-1
  fdm = 0.01d0
  fdm_hard = 0.05d0
  dt_softening_factor = 0.4

  implicit_scheme_tolerance = 1d-4
  max_tries_to_achieve = 200
  min_change_factor = 1.01d0
  max_change_factor = 1.2d0
  initial_change_factor = 1.2d0
  change_factor_fraction = 0.8d0
  implicit_lambda = 0.4d0

  min_mdot_for_implicit = 1d-9
  roche_min_mdot = 1d-10

  accretor_overflow_terminate = 100.0d0
  ! assume merger if mass transfer rate becomes too
    high
  max_implicit_abs_mdot = 0.1
/ ! end of binary_controls namelist

! inlist_header common for both components
&star_job
  show_log_description_at_start = .false.
  save_photo_when_terminate = .true.

  ! initial metal abundances
  relax_initial_Z = .true.
  new_Z = 0.014d0
  relax_initial_Y = .true.
  new_Y = 0.263d0
/ ! end of star_job namelist

&eos
/ ! end of eos namelist

&kap
  use_Type2_opacities = .true.
  Zbase = 0.0142d0
  kap_file_prefix = 'a09'
  kap_CO_prefix = 'a09_co'
  kap_lowT_prefix = 'lowT_fa05_a09p'
/ ! end of kap namelist

&controls
  ! output contrlons
  ! write_profiles_flag = .false.
  history_interval = 1
  photo_interval = 50000
  max_model_number = 50000
  max_number_retries = 5000
  photo_digits = 5

  ! convection
  use_leeloux_criterion = .true.
  mixing_length_alpha = 0.5
  alpha_seiconvection = 0.1
  thermohaline_coeff = 1

  ! Small amount of diffusive mixing to smooth the
    profiles including the Brunt-Vaisala frequency
    profile
  set_min_D_mix = .true.
  min_D_mix = 100.0 !10

  ! overshoot based on exponential formulation
  overshoot_scheme(1) = 'exponential'
  overshoot_zone_type(1) = 'burn_H'
  overshoot_zone_loc(1) = 'core'
  overshoot_bdy_loc(1) = 'top'
  overshoot_f(1) = 0.02
  overshoot_f0(1) = 0.001d0

  ! extra controls for timestep
  ! these are to properly resolve core hydrogen
    depletion
  delta_lg_XH_cntr_limit = 0.02d0
  delta_lg_XH_cntr_max = 0.0d0
  delta_lg_XH_cntr_min = -6.0d0
  ! these are to properly resolve core helium
    depletion
  delta_lg_XHe_cntr_limit = 0.02d0
  delta_lg_XHe_cntr_max = 0.0d0
  delta_lg_XHe_cntr_min = -6.0d0
  ! these are to properly resolve core carbon
    depletion
  delta_lg_XC_cntr_limit = 0.01d0
  delta_lg_XC_cntr_max = 0.0d0
  delta_lg_XC_cntr_min = -5.0d0
  ! controls for absolute changes in composition
  delta_XH_cntr_limit = 0.001d0

```

```

delta_XHe_cntr_limit = 0.001d0
delta_XC_cntr_limit = 0.001d0
! this is mainly to resolve properly when the star
  goes off the main sequence
delta_HR_limit = 0.005d0
! we're not looking for much precision at the very
  late stages
dX_nuc_drop_limit = 5d-2

retry_hold = 5
redo_limit = -1

! mesh
! extra spatial resolution
mesh_Pgas_div_P_exponent = 0.2
max_dq = 0.002
min_dq_for_xa = 1d-5
max_allowed_nz = 15000
mesh_delta_coeff = 0.2 !1.0
time_delta_coeff = 0.5 !1.0
num_cells_for_smooth_brunt_B = 10
threshold_for_smooth_brunt_B = 0.1
/ ! end of controls namelist

&pgstar
/ ! end of pgstar namelist

```


Appendix C: `GYRE` inlist

```

&constants
/
&model
  model_type = 'EVOL'
  file_format = 'MESA'
  file = 'LOGS/profile_h1_0.7.data.GYRE'
/
&mode
  l = 0
  tag = 'radial'
/
&mode
  l = 1
  tag = 'non-radial'
/
&mode
  l = 2
  tag = 'non-radial'
/
&mode
  l = 3
  tag = 'non-radial'
/
&mode
  l = 4
  tag = 'non-radial'
/
&osc
/
&rot
/
&num
  diff_scheme = 'MAGNUS_GL4'
/
&scan
  grid_type = 'LINEAR'
  freq_min = 1.0

```

```

  freq_max = 150.0
  n_freq = 200
  freq_units = 'CYC_PER_DAY'
  tag_list = 'radial'
/
&scan
  grid_type = 'INVERSE'
  freq_min = 0.1
  freq_max = 3.0
  n_freq = 1000
  freq_units = 'CYC_PER_DAY'
  tag_list = 'non-radial'
/
&scan
  grid_type = 'LINEAR'
  freq_min = 3.0
  freq_max = 150.0
  n_freq = 1000
  freq_units = 'CYC_PER_DAY'
  tag_list = 'non-radial'
/
&grid
  w_osc = 10
  w_exp = 2
  w_ctr = 10
/
&ad_output
  summary_file = 'LOGS/freqs_profile_h1_0.7.txt'
  summary_file_format = 'TXT'
  summary_item_list = 'l,n_pg,freq,freq_units'
  freq_units = 'CYC_PER_DAY'
/
&nad_output
/

```

Acknowledgements. This work was supported by the Polish National Science Centre (NCN), grant number 2021/43/B/ST9/02972. The research leading to these results has received funding from the European Research Council (ERC) under the Horizon Europe programme (Synergy Grant agreement No101071505: 4D-STAR). Calculations have been carried out using resources provided by Wrocław Centre for Networking and Supercomputing (<http://wcss.pl>), grant no. 265.

Data Availability

We make all files needed to recreate our MESA-BINARY and GYRE results publicly available at Zenodo:

TODO: link

Software

GYRE (Townsend & Teitler 2013; Townsend et al. 2018; Goldstein & Townsend 2020; Sun et al. 2023) MESA (Paxton et al. 2011, 2013, 2015, 2018, 2019; Jermyn et al. 2023), PYMESAREADER (https://billwolf.space/py_mesa_reader/index.html), PYTHON SciPy (Virtanen et al. 2020),

References

- Aerts, C., Christensen-Dalsgaard, J., & Kurtz, D. W. 2010, Asteroseismology (Springer)
- Arras, P., Townsley, D. M., & Bildsten, L. 2006, ApJ, 643, L119
- Asplund, M., Grevesse, N., Sauval, A. J., & Scott, P. 2009, ARA&A, 47, 481
- Basu, S., Antia, H. M., & Narasimha, D. 1994, MNRAS, 267, 209

- Brassard, P., Fontaine, G., Wesemael, F., Kawaler, S. D., & Tassoul, M. 1991, *ApJ*, 367, 601
- Buchler, J. R. & Yueh, W. R. 1976, *ApJ*, 210, 440
- Burssens, S., Bowman, D. M., Michelsen, M., et al. 2023, *Nature Astronomy*, 7, 913
- Cassisi, S., Potekhin, A. Y., Pietrinferni, A., Catelan, M., & Salaris, M. 2007, *ApJ*, 661, 1094
- Charpinet, S., Fontaine, G., Brassard, P., & Dorman, B. 2000, *ApJS*, 131, 223
- Chugunov, A. I., Dewitt, H. E., & Yakovlev, D. G. 2007, *Phys. Rev. D*, 76, 025028
- Cox, J. P. 1980, *Theory of Stellar Pulsation. (PSA-2)*, Volume 2, Vol. 2 (Princeton University Press)
- Cyburt, R. H., Amthor, A. M., Ferguson, R., et al. 2010, *ApJS*, 189, 240
- de Mink, S. E., Langer, N., Izzard, R. G., Sana, H., & de Koter, A. 2013, *ApJ*, 764, 166
- Duchêne, G. & Kraus, A. 2013, *ARA&A*, 51, 269
- Dziembowski, W. A. 1971, *Acta Astron.*, 21, 289
- Dziembowski, W. A., Moskalik, P., & Pamyatnykh, A. A. 1993, *MNRAS*, 265, 588
- Eggleton, P. P. 1983, *ApJ*, 268, 368
- Ferguson, J. W., Alexander, D. R., Allard, F., et al. 2005, *ApJ*, 623, 585
- Fuller, G. M., Fowler, W. A., & Newman, M. J. 1985, *ApJ*, 293, 1
- Goldstein, J. & Townsend, R. H. D. 2020, *ApJ*, 899, 116
- Gough, D. O. 1990, in *Progress of Seismology of the Sun and Stars*, ed. Y. Osaki & H. Shibahashi, Vol. 367, 283
- Guo, Z. 2021, *Frontiers in Astronomy and Space Sciences*, 8, 67
- Guo, Z., Gies, D. R., Matson, R. A., et al. 2017, *ApJ*, 837, 114
- Guo, Z. & Li, G. 2019, *ApJ*, 882, L5
- Guyot, N., Van Grootel, V., Charpinet, S., et al. 2025, *A&A*, 696, A13
- Henneco, J., Schneider, F. R. N., Hekker, S., & Aerts, C. 2024, *A&A*, 690, A65
- Henneco, J., Schneider, F. R. N., Heller, M., Hekker, S., & Aerts, C. 2025, arXiv e-prints, arXiv:2504.08683
- Herwig, F. 2000, *A&A*, 360, 952
- Iglesias, C. A. & Rogers, F. J. 1993, *ApJ*, 412, 752
- Iglesias, C. A. & Rogers, F. J. 1996, *ApJ*, 464, 943
- Irwin, A. W. 2004, *The FreeEOS Code for Calculating the Equation of State for Stellar Interiors*
- Itoh, N., Hayashi, H., Nishikawa, A., & Kohyama, Y. 1996, *ApJS*, 102, 411
- Jermyn, A. S., Bauer, E. B., Schwab, J., et al. 2023, *ApJS*, 265, 15
- Jerzykiewicz, M., Handler, G., Shobbrook, R. R., et al. 2005, *MNRAS*, 360, 619
- Kawaler, S. D., Winget, D. E., & Hansen, C. J. 1985, *ApJ*, 295, 547
- Kippenhahn, R., Ruschenplatt, G., & Thomas, H. C. 1980, *A&A*, 91, 175
- Kippenhahn, R. & Weigert, A. 1967, *ZAp*, 65, 251
- Kippenhahn, R. & Weigert, A. 1990, *Stellar Structure and Evolution* (Springer-Verlag)
- Koch, D. G., Borucki, W. J., Basri, G., et al. 2010, *ApJ*, 713, L79
- Kolb, U. & Ritter, H. 1990, *A&A*, 236, 385
- Kuhfuss, R. 1986, *A&A*, 160, 116
- Langanke, K. & Martínez-Pinedo, G. 2000, *Nuclear Physics A*, 673, 481
- Langer, N., El Eid, M. F., & Fricke, K. J. 1985, *A&A*, 145, 179
- Ledoux, P. 1947, *ApJ*, 105, 305
- Miglio, A., Montalbán, J., Noels, A., & Eggenberger, P. 2008, *MNRAS*, 386, 1487
- Miszuda, A. 2025, *Contributions of the Astronomical Observatory Skalnate Pleso*, 55, 196
- Miszuda, A., Kołaczek-Szymański, P. A., Szewczuk, W., & Daszyńska-Daszkiewicz, J. 2022, *MNRAS*, 514, 622
- Moe, M. & Di Stefano, R. 2017, *ApJS*, 230, 15
- Mombarg, J. S. G., Van Reeth, T., Pedersen, M. G., et al. 2019, *MNRAS*, 485, 3248
- Moravveji, E., Aerts, C., Pápics, P. I., Triana, S. A., & Vandoren, B. 2015, *A&A*, 580, A27
- Moravveji, E., Townsend, R. H. D., Aerts, C., & Mathis, S. 2016, *ApJ*, 823, 130
- Neo, S., Miyaji, S., Nomoto, K., & Sugimoto, D. 1977, *PASJ*, 29, 249
- Oda, T., Hino, M., Muto, K., Takahara, M., & Sato, K. 1994, *Atomic Data and Nuclear Data Tables*, 56, 231
- Ong, J. M. J., Lindsay, C. J., Reyes, C., Stello, D., & Roxburgh, I. W. 2025, *ApJ*, 980, 199
- Paxton, B., Bildsten, L., Dotter, A., et al. 2011, *ApJS*, 192, 3
- Paxton, B., Cantiello, M., Arras, P., et al. 2013, *ApJS*, 208, 4
- Paxton, B., Marchant, P., Schwab, J., et al. 2015, *ApJS*, 220, 15
- Paxton, B., Schwab, J., Bauer, E. B., et al. 2018, *ApJS*, 234, 34
- Paxton, B., Smolec, R., Schwab, J., et al. 2019, *ApJS*, 243, 10
- Pedersen, M. G., Aerts, C., Pápics, P. I., et al. 2021, *Nature Astronomy*, 5, 715
- Pedersen, M. G., Aerts, C., Pápics, P. I., & Rogers, T. M. 2018, *A&A*, 614, A128
- Podsiadlowski, P., Joss, P. C., & Hsu, J. J. L. 1992, *ApJ*, 391, 246
- Potekhin, A. Y. & Chabrier, G. 2010, *Contributions to Plasma Physics*, 50, 82
- Rauer, H., Catala, C., Aerts, C., et al. 2014, *Experimental Astronomy*, 38, 249
- Renzo, M. & Götzberg, Y. 2021, *ApJ*, 923, 277
- Renzo, M., Zapartas, E., de Mink, S. E., et al. 2019, *A&A*, 624, A66
- Renzo, M., Zapartas, E., Justham, S., et al. 2023, *ApJ*, 942, L32
- Reyes, C., Stello, D., Ong, J., et al. 2025, *Nature*, 640, 338
- Ricker, G. R., Winn, J. N., Vanderspek, R., et al. 2015, *Journal of Astronomical Telescopes, Instruments, and Systems*, 1, 014003
- Ritter, H. 1988, *A&A*, 202, 93
- Rogers, F. J. & Nayfonov, A. 2002, *ApJ*, 576, 1064
- Roxburgh, I. W. & Vorontsov, S. V. 1994, *MNRAS*, 267, 297
- Sana, H., de Mink, S. E., de Koter, A., et al. 2012, *Science*, 337, 444
- Saumon, D., Chabrier, G., & van Horn, H. M. 1995, *ApJS*, 99, 713
- Soberman, G. E., Phinney, E. S., & van den Heuvel, E. P. J. 1997, *A&A*, 327, 620
- Stankov, A. & Handler, G. 2005, *ApJS*, 158, 193
- Sun, M., Townsend, R. H. D., & Guo, Z. 2023, *ApJ*, 945, 43
- Tassoul, M. 1980, *ApJS*, 43, 469
- Timmes, F. X. & Swesty, F. D. 2000, *ApJS*, 126, 501
- Townsend, R. H. D., Goldstein, J., & Zweibel, E. G. 2018, *MNRAS*, 475, 879
- Townsend, R. H. D. & Kawaler, S. D. 2023, *Research Notes of the American Astronomical Society*, 7, 166
- Townsend, R. H. D. & Teitler, S. A. 2013, *MNRAS*, 435, 3406
- Verma, K., Faria, J. P., Antia, H. M., et al. 2014, *ApJ*, 790, 138
- Virtanen, P., Gommers, R., Oliphant, T. E., et al. 2020, *Nature Methods*, 17, 261
- Wagg, T., Johnston, C., Bellinger, E. P., et al. 2024, *A&A*, 687, A222
- White, T. R., Bedding, T. R., Stello, D., et al. 2011, *ApJ*, 743, 161
- Zwintz, K. & Steindl, T. 2022, *Frontiers in Astronomy and Space Sciences*, 9, 914738